

# Four-Switch Buck-Boost Integrated Bridge for Bidirectional Inductive Power Transfer With Hybrid Energy Storage System

Chunwei Ma<sup>ID</sup>, Graduate Student Member, IEEE, Xiaohui Qu<sup>ID</sup>, Senior Member, IEEE, Zhihao Guo<sup>ID</sup>, and Linlin Tan<sup>ID</sup>, Member, IEEE

**Abstract**—Hybrid energy storage systems (HESSs) with battery and supercapacitor (SC) are commonly used to cope with repeated power pulses in the wireless traffic energy Internet. Traditionally, converters with multiple power conversion stages are required for wireless charging of the HESS, increasing both the cost and losses. To address this issue, this article proposes a four-switch buck-boost (FSBB) integrated bridge that multiplexes the half-bridges in the FSBB topology for bidirectional inductive power transfer (BIPT) systems. Without adding additional power conversion stage, the proposed FSBB integrated bridge provides two dc ports for HESS and an ac port for BIPT system. This article also presents the modulation method for the FSBB integrated bridge and control strategy with optimal efficiency tracking for the BIPT system with HESS. With the proposed modulation method and control strategy, energy can flow freely and effectively among the battery, SC, and primary source of the BIPT system. A 150 W experimental prototype is provided to verify the effectiveness of the proposed FSBB integrated bridge for BIPT system with HESS.

**Index Terms**—Bidirectional inductive power transfer (BIPT), four-switch buck-boost (FSBB) integrated bridge, hybrid energy storage system (HESS).

## I. INTRODUCTION

As an alternative to the traditional plug-and-play charging method for electric vehicles (EVs), inductive power transfer (IPT) technology has undergone significant development in recent years [1], [2], [3]. The IPT system can effectively transfer power over short distances through weak magnetic coupling. Based on bidirectional IPT (BIPT) technology, novel concepts such as wireless traffic energy Internet [4], [5] and

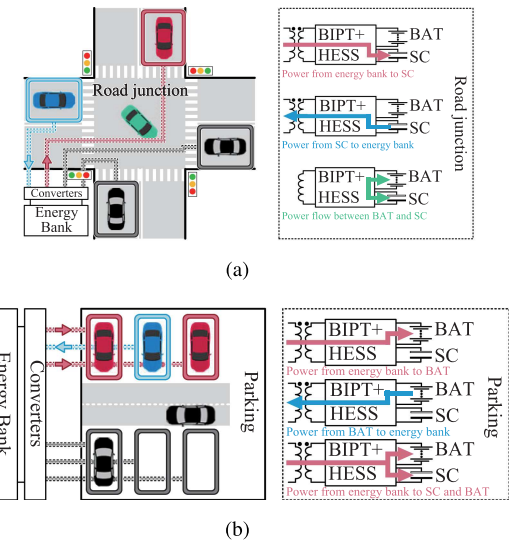


Fig. 1. Traffic energy Internet at: (a) road junction; and (b) parking.

electric roadway [6] have been proposed. As shown in Fig. 1, with coils set up at road junctions and parking, the wireless traffic energy Internet can realize bidirectional wireless grid-to-vehicle, vehicle-to-grid, and vehicle-to-vehicle energy trading during vehicle waiting time at traffic lights or charging time at parking to alleviate mileage anxiety of EVs and improve the power quality of the distribution grid [7].

However, the time a vehicle takes waiting over the coils at road junctions is relatively short. When driving through multiple intersections, the power electronics system of the EVs must process the high power pulses resulting from the repeated short-time wireless power transfer. Charging or discharging these high-power pulses directly into EVs' batteries results in excessive heating and degrades the life cycle of batteries [8]. Different from batteries that use chemical reactions for high energy density, the supercapacitor (SC) stores charges on two parallel plates separated by an insulator [9]. This gives SC higher power density and longer cycle life, making it suitable for handling repeated power pulses. Integrating battery and SC creates the hybrid energy storage system (HESS) with the complementary features of battery and SC [10], [11]. By optimizing

Received 28 July 2024; revised 23 December 2024; accepted 28 January 2025. This work was supported by the National Natural Science Foundation of China under Grant 52077038. (Corresponding author: Xiaohui Qu.)

The authors are with the School of Electrical Engineering, Southeast University, Nanjing 210096, China, and also with Jiangsu Key Laboratory of Smart Grid Technology and Equipment, Nanjing 210096, China (e-mail: xhqu@seu.edu.cn).

Digital Object Identifier 10.1109/TIE.2025.3541276

the proportion of battery and SC, the HESS can achieve higher power capability, larger energy storage, and longer cycle life in comparison with battery-only storage systems [12], [13]. As illustrated in Fig. 1(a), when EVs with HESS are waiting at the road junction, the high-power energy interactions can be addressed by the SC. As the vehicles move out of the coil range, the SC needs to be charged or discharged by the battery to prepare for the next power pulse. Meanwhile, when the vehicles are stopped in parking for a long period in Fig. 1(b), energy trading is realized between the energy bank and the battery.

To realize the power interaction among energy bank, SC, and battery, the EV's converter for wireless charging of HESS requires at least two dc ports for the HESS and an ac port for the IPT system. While, traditional active rectifiers such as half-bridge active rectifier, semiactive rectifier (SAR), and full-bridge active rectifier (FBAR) have only one dc port and one ac port. Therefore, integration of these three ports is usually achieved by cascading multiple topologies. In [14], the SC and battery are connected in parallel and linked to the output of the IPT system through a bidirectional buck-boost converter. This method requires only two stages of power conversion for transferring energy from coils to HESS. However, the voltage of battery and that of SC must be identical, making it impossible for the charging converter to modulate energy flow between SC and battery [11]. To achieve separate power control of battery and SC, both battery and SC of the HESSs in [15] and [16] are connected to the output of IPT system through a bidirectional dc–dc converter, necessitating at least three stages of power conversion. To reduce the number of power conversion stages, the SC in [17] is connected in parallel with the compensation capacitor of the IPT coils, and the energy of SC is regulated by controlling the dc voltage component of the compensation capacitor. While, the SC current is forced to flow through coils, resulting in inevitable power losses. With the help of boost active bridges, the wireless charging converter in [18] combines BIPT system and HESS using a single topology. However, two additional inductors are required, and SC's ability to handle power pulses is limited as voltage of SC must be less than that of battery.

For efficient bidirectional wireless charging of the HESS, a novel four-switch buck-boost (FSBB) integrated bridge is proposed in this article by multiplexing the two half-bridges in the FSBB topology. Compared to the conventional integration schemes with multiple stages, the FSBB integrated bridge requires only four MOSFETs and one inductor, and the power flow among the coil, battery, and SC only needs one energy conversion stage. This significantly improves the power density and efficiency of the system. Additionally, benefiting from the merit of FSBB topology's flexible dc voltage gain, the voltage of SC can exceed that of battery to handle bigger power pulse, and the ac voltage gain range is extended to  $[0, \sqrt{2}]$  to transfer more power between primary and secondary sides. The modulation method for the proposed FSBB integrated bridge and control strategy with optimal efficiency for the BIPT system of HESS is presented in this article as well. With the proposed modulation method and control strategy, energy can flow freely and effectively among the battery, SC, and the primary source.

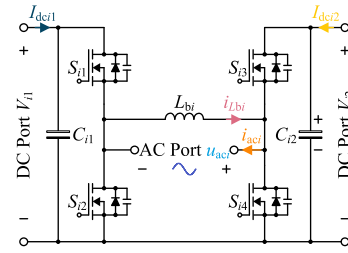


Fig. 2. Topology of FSBB integrated bridge.

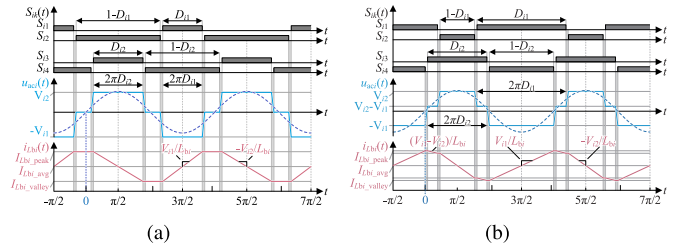


Fig. 3. Main waveforms of FSBB integrated bridge. (a)  $D_{i1} + D_{i2} \leq 1$ . (b)  $D_{i1} + D_{i2} > 1$ .

The rest of this article is organized as follows. The operation principle and voltage gains of the proposed FSBB integrated bridge are analyzed in Section II. Section III introduces the characteristics of the LCC–LCC BIPT system with FSBB integrated bridges for HESS. Modulation method and control strategy for the BIPT system are discussed in Section IV. The experimental results of a 150 W prototype are illustrated in Section V. Finally, Section VI concludes this article.

## II. TOPOLOGY OF FSBB INTEGRATED BRIDGE

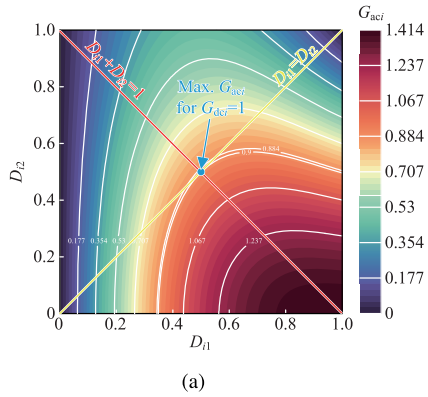
Fig. 2 illustrates the topology of the proposed FSBB integrated bridge, which consists of two half-bridges and an inductor. The inductor  $L_{bi}$  is connected to the midpoints of half-bridge formed by  $S_{i1}\&S_{i2}$  and half-bridge formed by  $S_{i3}\&S_{i4}$ . Obviously, this topology has two dc ports  $V_{i1}\&V_{i2}$ , and an ac port  $u_{aci}$ . Different from the conventional FSBB topology whose power flows only between the two dc ports, the FSBB integrated bridge can modulate the power among these three ports.

The main waveforms of the FSBB integrated bridge are illustrated in Fig. 3, where  $D_{i1}$  and  $D_{i2}$  are the duty cycles of  $S_{i1}$  and  $S_{i3}$ , respectively. The current of the inductor  $L_{bi}$  is continuous due to the synchronized operation of switches  $S_{i2}$  and  $S_{i4}$  [19]. Depending on whether the value of  $D_{i1} + D_{i2}$  is greater than unity, the FSBB integrated bridge has two operations, i.e.,  $D_{i1} + D_{i2} \leq 1$  and  $D_{i1} + D_{i2} > 1$ .

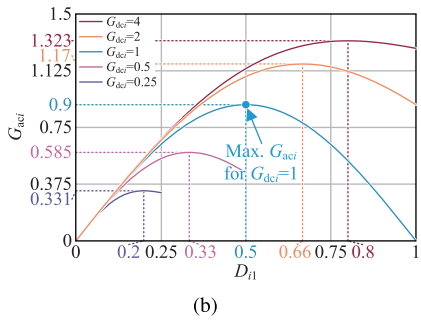
Based on the volt-second balance principle of the inductor  $L_{bi}$ , the dc voltage gain  $G_{dc1}$  can be derived as

$$G_{dc1} = \frac{V_{i2}}{V_{i1}} = \frac{D_{i1}}{D_{i2}}. \quad (1)$$

Applying Fourier analysis on the waveform of  $u_{aci}$  in Fig. 3, the ac voltage gain  $G_{aci}$  between root mean square (rms) value



(a)



(b)

**Fig. 4.** (a) Variation trend of  $G_{aci}$  with  $D_{i1}$  and  $D_{i2}$ . (b) Variation trend of  $G_{aci}$  with  $D_{i1}$  at the given  $G_{dci}$ .

of the ac voltage fundamental component  $U_{aci}$  and  $V_{i1}$  can be deduced as

$$G_{aci} = \frac{U_{aci}}{V_{i1}} = \frac{\sqrt{2}}{\pi} \frac{(D_{i1} \sin \pi D_{i2} + D_{i2} \sin \pi D_{i1})}{D_{i2}}. \quad (2)$$

Fig. 4(a) demonstrates the variation trend of  $G_{aci}$  with  $D_{i1}$  and  $D_{i2}$ . It is clear that the maximum value of  $G_{aci}$  is  $\lim_{D_{i1} \rightarrow 1, D_{i2} \rightarrow 0} G_{aci} = \sqrt{2}$ . Thus, the maximum ac voltage gain of FSBB integrated bridge is  $\sqrt{2} \approx 1.414$  which is about 1.57 times compared with that of the conventional full-bridge [20].

Also, it can be observed that a given  $G_{aci}$  may result in diverse combinations of  $D_{i1}$  and  $D_{i2}$ , which leads to different  $G_{dci}$ . Fig. 4(b) exhibits the variation trend of  $G_{aci}$  with  $D_{i1}$  at the given  $G_{dci}$ . Obviously, as  $D_{i1}$  increases,  $G_{aci}$  first increases and then decreases. By combining (1) and (2) and solving for the derivation, it can be determined that the maximum  $G_{aci}$  is attained when  $D_{i1} + D_{i2} = 1$ . Similarly, it can be deduced that for a given  $G_{aci}$ , the minimum  $G_{dci}$  is obtained when the condition  $D_{i1} + D_{i2} = 1$  is satisfied as well. The intersection point ( $D_{i1} = 0.5$ ,  $D_{i2} = 0.5$ ) of the line  $D_{i1} + D_{i2} = 1$  with the line  $D_{i1} = D_{i2}$  ( $G_{dci} = 1$ ) in Fig. 4(a) is exactly the point of tangency between line  $G_{aci} = 0.9$  and line  $D_{i1} = D_{i2}$ , proving the above conclusion. Thus, when  $D_{i1} + D_{i2} \leq 1$ , both  $G_{aci}$  with a given  $G_{dci}$  and  $G_{dci}$  with a given  $G_{aci}$  have monotony variation trend with  $D_{i1}$ . To achieve better control, the modulation of the FSBB integrated bridge in this article always satisfies the condition  $D_{i1} + D_{i2} \leq 1$ .

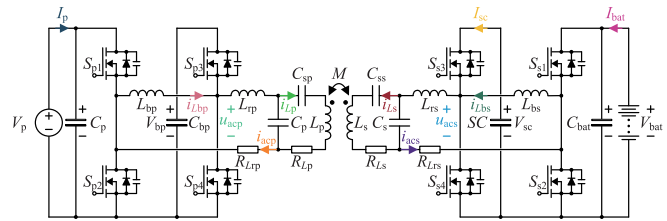


**Fig. 5.** Topology of the LCC–LCC BIPT system with FSBB integrated bridges for HESS.

### III. CHARACTERISTICS OF LCC–LCC BIPT SYSTEM WITH FSBB INTEGRATED BRIDGE FOR HESS

Fig. 5 shows the circuit topology of the BIPT system with two FSBB integrated bridges. For the primary FSBB integrated bridge where  $i = p$ , the primary voltage source  $V_p$  is connected to the dc port  $V_{p1}$ , and the dc port  $V_{p2}$  is not connected to any load or source. On the secondary side where  $i = s$ , the battery and SC of the HESS are connected to the  $V_{s1}$  and  $V_{s2}$  of the secondary FSBB integrated bridge, respectively. Both the primary and secondary resonant cavities are connected to the ac ports  $u_{acp,s}$  of the FSBB integrated bridges. The magnetic coupler has primary self-inductance  $L_p$ , secondary self-inductance  $L_s$ , and mutual inductance  $M$ . The coupling coefficient is defined as  $k = M / \sqrt{L_p L_s}$ . Due to the advantages of constant coil current and high power transfer capacity, the LCC–LCC compensation network is chosen as the resonant compensation network in the BIPT system [21].  $L_{rp}$ ,  $C_p$ , and  $C_{sp}$  are the compensation components of primary coil,  $L_{rs}$ ,  $C_s$ , and  $C_{ss}$  are the compensation components of secondary coil. The parameters of these compensation components are designed as

$$\begin{cases} \omega L_{rp} = \frac{1}{\omega C_p} = \omega L_p - \frac{1}{\omega C_{sp}} \\ \omega L_{rs} = \frac{1}{\omega C_s} = \omega L_s - \frac{1}{\omega C_{ss}}. \end{cases} \quad (3)$$

where  $\omega = 2\pi f_s$  and  $f_s$  is the resonant frequency as well as the switching frequency of the system. Coils' losses are represented by equivalent series resistances (ESRs)  $R_{Lp}$  and  $R_{Ls}$ , and  $R_{Lrp}$  and  $R_{Lrs}$  are the equivalent loss resistances of the compensation inductors branches. It is noteworthy that when the primary circuit is removed, the secondary LCC compensation network exhibits open circuit characteristic so that power can be modulated between the battery and SC.

#### A. Power Profile of the BIPT System

As the high-order harmonics has little contribution to the power transfer due to the resonance operation, the transferred power of the LCC–LCC BIPT system is mainly related to the fundamental component. Fig. 6 depicts the decoupled fundamental harmonic approximation (FHA) equivalent circuit of the BIPT system with FSBB integrated bridges. According to (2), the rms fundamental component ac voltage of primary side  $U_{acp}$  and that of secondary side  $U_{acs}$  are

$$U_{acp} = G_{acp} V_p \angle 0, \quad U_{acs} = G_{acs} V_{bat} \angle \theta \quad (4)$$

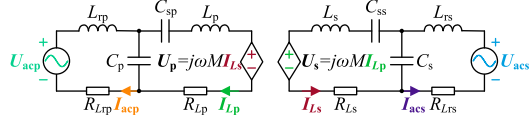


**Fig. 6.** Decoupled FHA equivalent circuit of LCC–LCC BIPT system with FSBB integrated bridges.

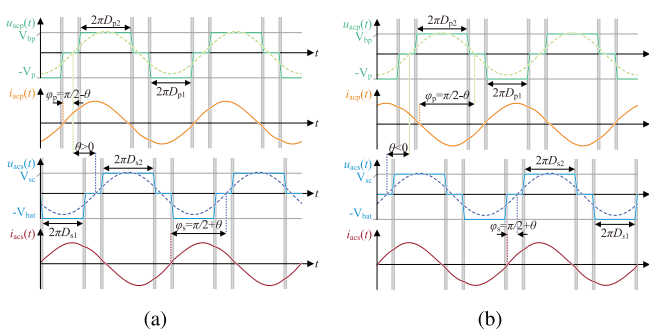


**Fig. 7.** Main waveforms of LCC–LCC BIPT system with FSBB integrated bridges. (a) Forward active power transfer with  $\theta > 0$ . (b) Backward active power transfer with  $\theta < 0$ .

where  $\theta$  is the phase angle between  $\mathbf{U}_{\text{acp}}$  and  $\mathbf{U}_{\text{acs}}$ . Based on Kirchhoff's voltage law, the fundamental component currents of the resonant tank can be obtained as

$$\begin{aligned} \mathbf{I}_{Lp} &= \frac{\mathbf{U}_{\text{acp}}}{j\omega L_{\text{rp}}}, & \mathbf{I}_{\text{acp}} &= \frac{-M\mathbf{U}_{\text{acs}}}{j\omega L_{\text{rp}}L_{\text{rs}}} \\ \mathbf{I}_{Ls} &= \frac{\mathbf{U}_{\text{acs}}}{j\omega L_{\text{rs}}}, & \mathbf{I}_{\text{acs}} &= \frac{-M\mathbf{U}_{\text{acp}}}{j\omega L_{\text{rp}}L_{\text{rs}}}. \end{aligned} \quad (5)$$

The main fundamental harmonic waveforms of the BIPT system are plotted in Fig. 7, where  $\varphi_p = \pi/2 - \theta$  is phase angle of  $u_{\text{acp}}$  lagging  $i_{\text{acp}}$ , and  $\varphi_s = \pi/2 + \theta$  is phase angle of  $u_{\text{acs}}$  lagging  $i_{\text{acs}}$ . Neglecting the loss resistances, the transferred active power  $P_{\text{ac}}$  and reactive power  $Q_{\text{ac}}$  are calculated as

$$\begin{cases} P_{\text{ac}} = \frac{M}{\omega L_{\text{rp}}L_{\text{rs}}} G_{\text{acp}} G_{\text{acs}} V_p V_{\text{bat}} \sin \theta, \\ Q_{\text{ac}} = \frac{M}{\omega L_{\text{rp}}L_{\text{rs}}} G_{\text{acp}} G_{\text{acs}} V_p V_{\text{bat}} \cos \theta. \end{cases} \quad (6)$$

Thus, the transmitted power from primary side to secondary side can be modulated by both the ac voltage gain of the primary FSBB integrated bridge  $G_{\text{acp}}$  and that of secondary FSBB integrated bridge  $G_{\text{acs}}$ . In addition, when  $0 < \theta < \pi$ , active power is transferred from primary side to secondary side. While, when  $-\pi < \theta < 0$ , the power flow is reversed. The maximum active power transfer is achieved when  $\theta$  is  $\pi/2$  or  $-\pi/2$ , where

$$i_{\text{acp,s}}(t) = \begin{cases} -\frac{\pi D_{p,s1} V_{p,s1}}{\omega L_{\text{rp,s}}} + \frac{\sqrt{2}G_{\text{acp,s}}V_{p,s1}}{\omega L_{\text{rp,s}}} \cos(\omega t) + \frac{\sqrt{2}P_{\text{ac}}}{G_{\text{acp,s}}V_{p,s1}\sin\theta} \cos(\omega t + \delta) & \frac{-\pi+2\pi D_{p,s1}}{2\omega} \leq t < \frac{\pi-2\pi D_{p,s1}}{2\omega} \\ \frac{V_{p,s2}}{\omega L_{\text{rp,s}}} (\omega t - \frac{\pi}{2}) + \frac{\sqrt{2}G_{\text{acp,s}}V_{p,s1}}{\omega L_{\text{rp,s}}} \cos(\omega t) + \frac{\sqrt{2}P_{\text{ac}}}{G_{\text{acp,s}}V_{p,s1}\sin\theta} \cos(\omega t + \delta) & \frac{\pi-2\pi D_{p,s2}}{2\omega} \leq t < \frac{\pi+2\pi D_{p,s2}}{2\omega} \\ \frac{\pi D_{p,s1} V_{p,s1}}{\omega L_{\text{rp,s}}} + \frac{\sqrt{2}G_{\text{acp,s}}V_{p,s1}}{\omega L_{\text{rp,s}}} \cos(\omega t) + \frac{\sqrt{2}P_{\text{ac}}}{G_{\text{acp,s}}V_{p,s1}\sin\theta} \cos(\omega t + \delta) & \frac{\pi+2\pi D_{p,s2}}{2\omega} \leq t < \frac{3\pi-2\pi D_{p,s1}}{2\omega} \\ \frac{V_{p,s1}}{\omega L_{\text{rp,s}}} (\frac{3\pi}{2} - \omega t) + \frac{\sqrt{2}G_{\text{acp,s}}V_{p,s1}}{\omega L_{\text{rp,s}}} \cos(\omega t) + \frac{\sqrt{2}P_{\text{ac}}}{G_{\text{acp,s}}V_{p,s1}\sin\theta} \cos(\omega t + \delta) & \frac{3\pi-2\pi D_{p,s1}}{2\omega} \leq t < \frac{3\pi+2\pi D_{p,s1}}{2\omega} \end{cases} \quad (12)$$

the reactive power is minimized. To reduce the volt–ampere requirements of the MOSFETs and obtain higher efficiency, the phase angle  $\theta$  is set to  $\pm\pi/2$  in this article.

Assuming  $R_{Lp} = R_{Ls} = R$ ,  $R_{Lrp} = R_{Lrs} = R_r$ ,  $(L_p/L_{\text{rp}}) = (L_s/L_{\text{rs}}) = \alpha$ ,  $\omega L_{\text{rp}} = \omega L_{\text{rs}} = X$ , and  $(U_{\text{acs}}/U_{\text{acp}}) = \lambda$  due to the symmetrical system, the efficiency of LCC–LCC resonant tank  $\eta$  can be derived as

$$\eta = \frac{\alpha k X \lambda}{\alpha k X \lambda + (\alpha^2 k^2 R_r + R) \lambda^2 + \alpha^2 k^2 R_r + R}. \quad (7)$$

By solving the derivation of  $\eta$  with respect to  $\lambda$ , the optimal excitation voltage ratio  $\lambda_{\text{opt}}$  to obtain the maximum efficiency of the resonant tank can be deduced as

$$\frac{d\eta}{d\lambda} = 0 \Rightarrow \lambda_{\text{opt}} = \frac{U_{\text{acp}}}{U_{\text{acs}}} = 1 \Rightarrow \frac{G_{\text{acp}}}{G_{\text{acs}}} = \frac{V_{\text{bat}}}{V_p}. \quad (8)$$

Since the charging and discharging time of SC is much shorter than that of battery, it is justified to consider that the voltage of battery  $V_{\text{bat}}$  is rigid. According to the characteristics of capacitors and analysis in Section II, the charging and discharging power of the SC can be deduced as

$$P_{\text{sc}} = I_{\text{sc}} V_{\text{sc}} = C_{\text{sc}} \frac{dV_{\text{sc}}}{dt} V_{\text{sc}} = \frac{dG_{\text{dcs}}}{dt} V_{\text{bat}} C_{\text{sc}} V_{\text{sc}}. \quad (9)$$

It is clear that the power of the SC can be controlled by the dc voltage gain of the secondary FSSB integrated bridge  $G_{\text{dcs}}$ . Based on the energy conservation principle of the secondary FSBB integrated bridge, the power flow among the battery, SC, and BIPT system always satisfies the following:

$$P_{\text{bat}} = P_{\text{ac}} - P_{\text{sc}}. \quad (10)$$

Therefore, the power control of the battery can be realized by adjusting the power of the BIPT system in (6) and the power of the SC in (9). Specifically, when  $P_{\text{ac}} = P_{\text{sc}}$ , the SC will take all power from the primary source. While, if  $P_{\text{ac}} \neq P_{\text{sc}}$ , the battery will act as a regulator, absorbing or compensating for the power difference between  $P_{\text{ac}}$  and  $P_{\text{sc}}$ .

## B. Soft-Switching Characteristics and Current Stresses of MOSFETs

According to the waveforms in Fig. 3(a), the conditions for zero-voltage switching (ZVS) turn-ON of MOSFETs  $S_{p,s1}$ – $S_{p,s4}$  can be deduced as

$$\begin{aligned} I_{\text{ac\_sp},s1} &\geq I_{\text{Lbp,s\_valley}}, & I_{\text{ac\_sp},s2} &\leq I_{\text{Lbp,s\_peak}} \\ I_{\text{ac\_sp},s3} &\leq I_{\text{Lbp,s\_peak}}, & I_{\text{ac\_sp},s4} &\geq I_{\text{Lbp,s\_valley}} \end{aligned} \quad (11)$$

where  $I_{\text{ac\_sp},sk}$  ( $k = 1, 2, 3$ , and  $4$ ) is instantaneous value of  $i_{\text{acp,s}}$  in deadband prior to corresponding MOSFET's conduction.

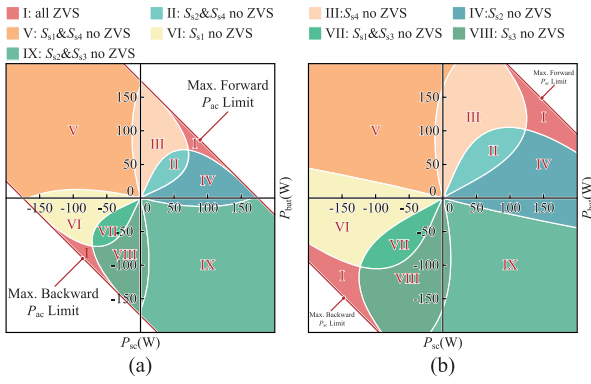


**Fig. 8.** ZVS region division in power distribution diagram. (a)  $V_{sc} = 48$  V. (b)  $V_{sc} = 96$  V.

Since  $i_{acp,s}$  contains many high-order harmonics in the LCC–LCC topology, the calculation of  $i_{acp,s}$ 's instantaneous expression requires the square wave excitation voltages, which leads to complex high-order differential equations. Fortunately, due to the filtering function of  $L_{rp,s}$  and  $C_{p,s}$ , the voltages across  $C_{p,s}$  are free from high-order harmonics and can be deduced by the FHA method based on (5) to simplify the calculation process [22]. Thus, by solving the differential equations for  $L_{rp,s}$ , the instantaneous expression of  $i_{acp,s}$  can be derived as (12) as shown at the bottom of the previous page, where  $\delta = -\theta$  for primary side and  $\delta = \theta$  for secondary side. Bring the turn-ON time of the MOSFETs  $t_{0,sp,sk}$  into (12), the  $I_{ac,sp,sk}$  in (11) can be determined. From Fig. 3,  $t_{0,sp,sk}$  is equal to  $(3\pi - 2\pi D_{p,s1}/2\omega)$ ,  $(-\pi + 2\pi D_{p,s1}/2\omega)$ ,  $(\pi - 2\pi D_{p,s2}/2\omega)$ , and  $(\pi + 2\pi D_{p,s2}/2\omega)$  for  $S_{p,s1}-S_{p,s4}$ , respectively.

Based on the waveform of inductor current in Fig. 3, the inductors' average current  $I_{Lbp,s\_avg}$  can be deduced as

$$I_{Lbp,s\_avg} = -\frac{I_{dcp,s2}}{D_{p,s2}} + \sqrt{2}I_{acp,s} \frac{\sin \pi D_{p,s2}}{\pi D_{p,s2}} \cos \varphi_{p,s}. \quad (13)$$

As  $D_{p,s1} + D_{p,s2} \leq 1$  is always satisfied, the inductor's peak current  $I_{Lbp,s\_peak}$  is  $I_{Lbp,s\_avg} + (V_{p,s1}D_{p,s1}/2f_s L_{bp,s})$  and the inductor's valley current  $I_{Lbp,s\_valley}$  is  $I_{Lbp,s\_avg} - (V_{p,s1}D_{p,s1}/2f_s L_{bp,s})$ .

According to (11)–(13), it can be deduced that the ZVS turn-on conditions for the primary MOSFETs  $S_{p1}-S_{p4}$  are all satisfied with the special modulation method  $D_{p1} + D_{p2} = 1$  stated in Section IV-A. Consequently, MOSFETs of the primary FSBB integrated bridge can always achieve ZVS turn-on.

The soft-switching characteristics of the secondary FSBB integrated bridge can be analyzed using the power distribution diagram in Fig. 8, where the horizontal axis represents the power discharged by battery and vertical axis represents the power discharged by the SC. On the basis of (11)–(13) and parameters in Table I, the power distribution diagram is divided into nine regions. It is evident that the ZVS turn-on of all MOSFETs can only be realized in region I of Fig. 8. Nevertheless, it is noteworthy that the BIPT system has at most two MOSFETs in the hard-switching state without introducing reactive power.

**TABLE I**  
PARAMETERS OF THE EXPERIMENTAL PROTOTYPE

Symbols	Parameters	Values
$V_p$	Input voltage	48 V
$V_{bat}$	Battery voltage	48 V
$V_{sc}$	SC voltage range	48–96 V
$f_s$	Inverter frequency	85 kHz
$L_p$	Self-inductance of primary coil	161.36 $\mu$ H
$R_p$	ESR of primary coil	191.26 m $\Omega$
$L_{rp}$	Primary compensation inductor	31.43 $\mu$ H
$C_p$	Primary parallel compensation capacitor	109.85 nF
$C_{sp}$	Primary series compensation capacitor	26.96 nF
$L_{bp}$	Primary bridge inductor	30 $\mu$ H
$L_s$	Self-inductance of secondary coil	161.396 $\mu$ H
$R_s$	ESR of secondary coil	195.51 m $\Omega$
$L_{rs}$	Secondary compensation inductor	30.71 $\mu$ H
$C_s$	Secondary parallel compensation capacitor	112.64 nF
$C_{ss}$	Secondary series compensation capacitor	26.95 nF
$L_{bs}$	Secondary bridge inductor	50 $\mu$ H
$k$	Coupling coefficient	0.3

The rms currents of the MOSFETs  $I_{sp,sk}$  in the BIPT system can be calculated as

$$I_{sp,sk} = \sqrt{\frac{\int_{t_{0,sp,sk}}^{t_{0,sp,sk} + \frac{2\pi D_{p,sk}}{\omega}} [i_{acp,s}(t) - i_{Lbp,s}(t - t_{0,sp,sk})]^2 dt}{T_s}} \quad (14)$$

where  $D_{p,sk}$  is the duty cycle for corresponding MOSFET. According to Fig. 3(a),  $D_{p,sk}$  is equal to  $D_{p,s1}$ ,  $1 - D_{p,s1}$ ,  $D_{p,s2}$ , and  $1 - D_{p,s2}$  for MOSFETs  $S_{p,s1}-S_{p,s4}$ , respectively. By substituting (12) into (14), the rms currents of the MOSFETs in the BIPT system when  $V_{sc} = 96$  V are illustrated in Fig. 9. Since the condition  $D_{p1} + D_{p2} = 1$  is always satisfied for the primary FSBB integrated bridge, the rms currents of  $S_{p1}$  and  $S_{p3}$  are equal to that of  $S_{p4}$  and  $S_{p2}$ , respectively. In addition, it can be noticed from Fig. 9(a) that the current stress of MOSFETs  $S_{p2}$  and  $S_{p3}$  is much smaller than that of  $S_{p1}$  and  $S_{p4}$  as the dc port  $V_{p2}$  is not connected to any source or load. From Fig. 9(b) and 9(c), it is obvious that the maximum current stresses of the secondary MOSFETs occur along the minor diagonal where  $P_{sc} = -P_{bat}$ . While, when  $P_{sc} = P_{bat}$ , the current stresses of the MOSFETs decrease significantly.

#### IV. CONTROL STRATEGY

##### A. Control Strategy for Power Transfer Among Source, SC, and Battery

As the constant power (CP) charging mode has the advantages of higher charging rate, no excessive thermal design, and avoiding faster degradation at high charging rates [23], the CP charging profile is employed for both SC and battery in the HESS. Fig. 10 illustrates the control diagram of the proposed BIPT system with FSBB integrated bridges for HESS, which has three control objectives: 1) the charging and discharging power of the SC; 2) the charging and discharging power of the battery; and 3) the optimal excitation voltage ratio  $\lambda_{opt}$  of the resonant tank.

Since the primary side is just connected to the input voltage source  $V_p$ , only  $G_{acp}$  needs to be regulated for the primary FSBB integrated bridge to achieve the optimal efficiency

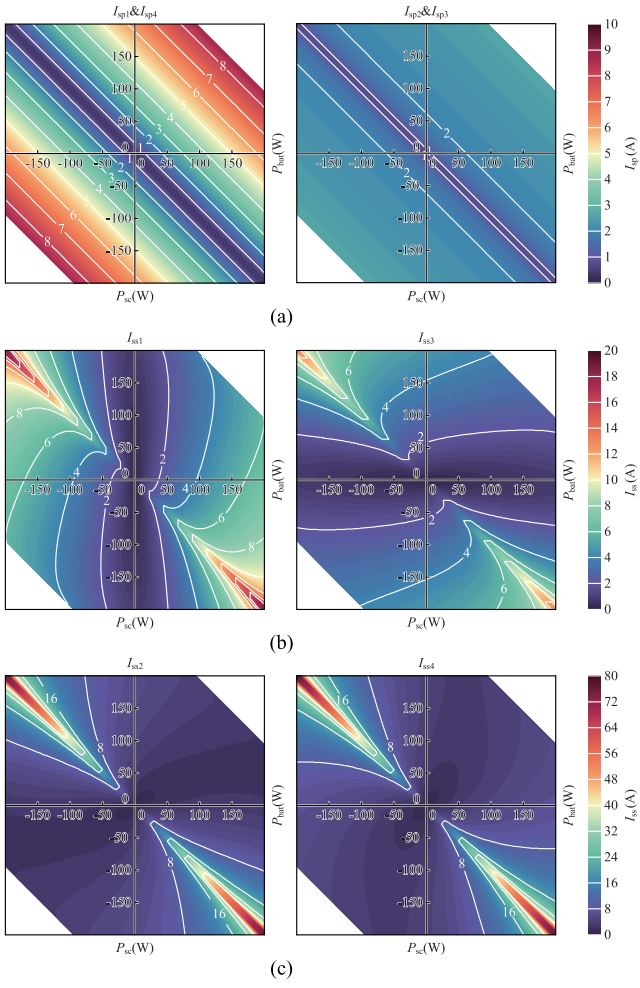


**Fig. 9.** RMS currents of the MOSFETs in power distribution diagram when  $V_{\text{sc}} = 96$  V. (a) MOSFETs  $S_{\text{p}1}$ – $S_{\text{p}4}$ . (b) MOSFETs  $S_{\text{s}1}$  and  $S_{\text{s}3}$ . (c) MOSFETs  $S_{\text{s}2}$  and  $S_{\text{s}4}$ .

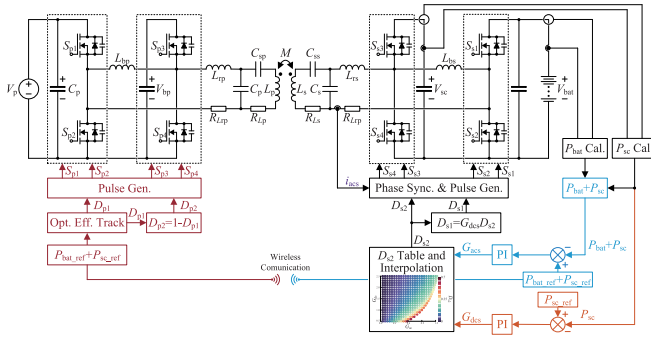


**Fig. 10.** Control strategy for power transfer among primary source, SC, and battery.

tracking of the resonant network. To simplify the control, the complementary condition  $D_{\text{p}1} + D_{\text{p}2} = 1$  is always satisfied. Fig. 11(a) shows the monotonic trend of  $G_{\text{acp}}$  with  $D_{\text{p}2} = 1 - D_{\text{p}1}$ . In addition, as illustrated in Fig. 4(a), for a given  $G_{\text{acp}}$ , the minimum  $G_{\text{dep}}$  is achieved when  $D_{\text{p}1} + D_{\text{p}2} = 1$ . Thus, this complementary modulation method can minimize the voltage

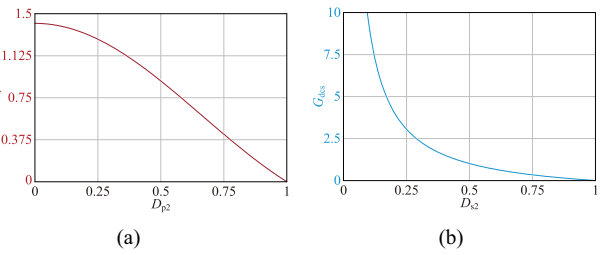


**Fig. 11.** (a) Variation trend of  $G_{\text{acp}}$  with  $D_{\text{p}2} = 1 - D_{\text{p}1}$ . (b) Variation trend of  $G_{\text{dcs}}$  with  $D_{\text{s}2} = 1 - D_{\text{s}1}$ .

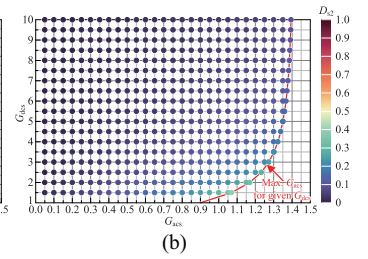


**Fig. 12.**  $D_{\text{s}2}$  look-up table for given  $G_{\text{acs}}$  and  $G_{\text{dcs}}$ . (a)  $0 < G_{\text{dcs}} \leq 1$ . (b)  $1 < G_{\text{dcs}} \leq 10$ .

stresses on MOSFETs  $S_{\text{p}3}$  and  $S_{\text{p}4}$ . The required transfer power  $P_{\text{ac}} = P_{\text{sc}} + P_{\text{bat}}$  for calculation of the optimal  $G_{\text{acp}}$  is achieved from the secondary side through the wireless communication methods such as LoRa and Bluetooth. It is noteworthy that the wireless communication between primary and secondary sides does not affect the stability of system, as it is not involved in the real-time control strategy.

For the secondary FSBB integrate bridge, the ac voltage gain  $G_{\text{acs}}$  and the dc voltage gain  $G_{\text{dcs}}$  should be regulated simultaneously to control the power flow among primary source, SC, and battery. Ideally, the  $D_{\text{s}1}$  and  $D_{\text{s}2}$  for a given  $G_{\text{acs}}$  and  $G_{\text{dcs}}$  can be solved by combining (1) and (2). Unfortunately, (2) is a transcendental function that cannot be solved analytically. As an alternative, the  $D_{\text{s}2}$  for given  $G_{\text{acs}}$  and  $G_{\text{dcs}}$  is numerically solved by the Newton–Raphson method with mathematical calculation software and plotted in Fig. 12. In this figure, the red line satisfies the critical condition  $D_{\text{s}1} + D_{\text{s}2} = 1$  and represents the maximum  $G_{\text{acs}}$  for a given  $G_{\text{dcs}}$  or the minimum  $G_{\text{dcs}}$  for a given  $G_{\text{acs}}$ . It is obvious that  $D_{\text{s}2}$  decreases monotonically with  $G_{\text{dcs}}$  and increases monotonically with  $G_{\text{acs}}$ . Therefore, based on Fig. 12, the  $G_{\text{acs}}$  and  $G_{\text{dcs}}$  can be effectively modulated by look-up table and interpolation method that has been widely adopted for the conventional FSBB converter [24].

To ensure tight control of the battery's power and SC's power, the control strategy of the secondary FSBB integrated bridge in Fig. 10 is mainly comprised of two proportion–integration (PI) control loops: the SC power loop and the ac power loop. The SC power loop is used to modulate the SC's power based on (9), while the ac power loop is employed to control the battery's power according to (10). The synchronization between the primary and secondary sides is achieved with the circuit in

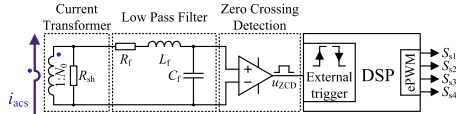


Fig. 13. Synchronization circuit between primary and secondary sides.

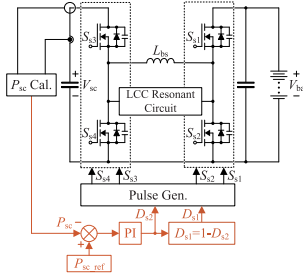


Fig. 14. Control strategy for power transfer between SC and battery when primary circuit is removed.

Fig. 13, which is composed of a current transformer, a low-pass filter, and an ultrafast amplifier. Simulation of the BIPT system operating at the rated power shows that the open loop gains of the system with these two control loops have phase margins greater than  $60^\circ$  with crossover frequencies at about 40 Hz. Therefore, the system with these two control loops is stable.

### B. Control Strategy When Primary Circuit Is Removed

When the primary circuit is removed, the secondary FSBB integrated bridge needs to modulate the power flowing between the SC and the battery of HESS. Fig. 14 exhibits the control diagram of the secondary FSBB integrated bridge when primary circuit is removed. As the secondary LCC compensation network can be treated as an open circuit when primary circuit is removed, the power flow between battery and SC can be controlled by only regulating the  $G_{\text{dcs}}$ . The complementary modulation condition  $D_{s1} + D_{s2} = 1$  is satisfied in this operation mode as well to simplify the control, and Fig. 11(b) illustrates the monotonic trend of  $G_{\text{dcs}}$  with  $D_{s2} = 1 - D_{s1}$ . To tight control the SC's power, the  $G_{\text{dcs}}$  is regulated by a simple PI control loop as well.

## V. EXPERIMENT VERIFICATION

To verify the analysis and performance of the proposed BIPT system with FSBB integrated bridges for HESS, a hardware prototype is built in the laboratory as shown in Fig. 15. The popular circular pad magnetic coupler with an outer diameter of 240 mm is adopted in this article. Both the primary and secondary coils are wound 32 turns with Litz wire of size  $0.1 \times 300$  mm. The transfer distance is 66 mm at coupling coefficient of 0.3. Precise parameters of the prototype are measured by the impedance analyzer and listed in Table I. The prototype is controlled by the DSP TMS320F28335, and the MOSFETs of the FSBB bridges are MOT7146T. All waveforms are recorded

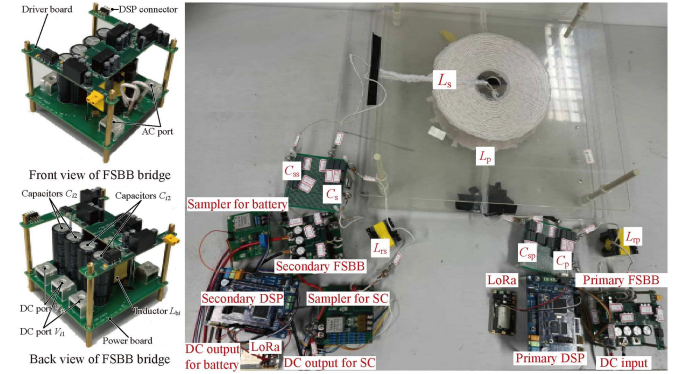
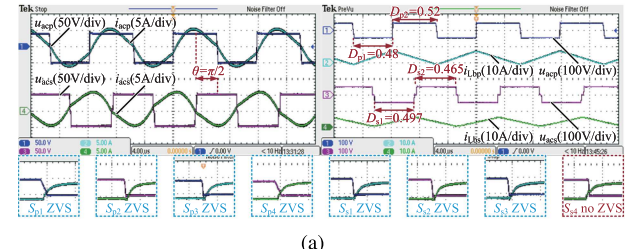
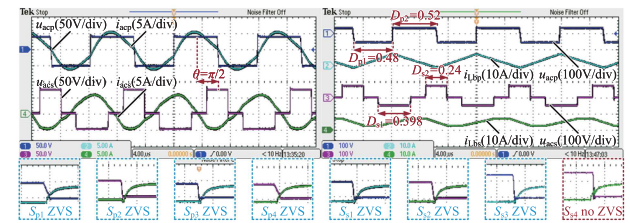


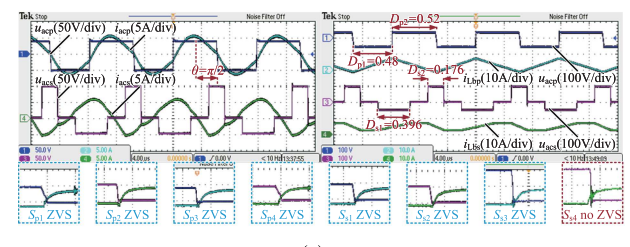
Fig. 15. Hardware prototype of BIPT system with FSBB integrated bridges for HESS.



(a)



(b)



(c)

Fig. 16. Experimental waveforms at: (a) beginning ( $V_{\text{sc}} = 48$  V); (b) middle ( $V_{\text{sc}} = 72$  V); and (c) end ( $V_{\text{sc}} = 96$  V) of 150 W SC charging process.

by Tektronix DPO 2024 Oscilloscope. Power and efficiency are measured by YOKOGAWA WT1085E.

### A. Experimental Waveforms

1) *SC Charging*: Fig. 16 exhibits the experimental waveforms of primary voltage  $u_{\text{acp}}$ , primary current  $i_{\text{acp}}$ , primary inductor current  $i_{L_{\text{bp}}}$ , secondary voltage  $u_{\text{acs}}$ , secondary current  $i_{\text{acs}}$ , and secondary inductor current  $i_{L_{\text{bs}}}$  at the beginning, middle, and end of the primary source charging SC process. For the forward power transfer, the phase angle  $\theta$  is kept at

$\pi/2$ . Thus, the voltage  $u_{acp}$  and current  $i_{acp}$  on the primary side are in phase, and the voltage  $u_{acs}$  is in opposite phase to current  $i_{acs}$  on the secondary side. The duty cycles  $D_{p1}$  and  $D_{p2}$  of primary FSBB integrate bridge are kept at 0.48 and 0.52 throughout the charging process with the constant 150 W charging power. According to (13), the average current of the primary bridge inductor  $I_{Lbp\_avg}$  is greater than 0 when the power is transferred forward. As the charging proceeds, the dc voltage gain of secondary FSBB integrated bridge  $G_{dcs}$  increases with the SC's terminal voltage  $V_{sc}$ , and the ac voltage gain  $G_{acs}$  is sustained around 0.94 to maintain the 150 W active power from the primary source. As all power flows into SC, the average current of the secondary bridge inductor  $L_{bs}$  is greater than 0 as well. In addition, it is worth noting that the ZVS turn-on of all MOSFETs except  $S_{s4}$  can be achieved throughout the SC charging process without introducing reactive power. This is consistent with the soft-switching analysis in Section III-B.

2) *Battery Charging*: Fig. 17 illustrates the experimental waveforms of the battery charging with different charging powers. In this mode, the energy flows from the primary source to the battery. For the primary FSBB integrated bridge,  $D_{p1}$  reduces from 0.48 to 0.33 as the charging power decreases, and  $D_{p2}$  increases from 0.52 to 0.67 for the complementary modulation. As no energy flows into the SC, the terminal voltage  $V_{sc}$  is kept at 48 V, and the dc voltage gain of the secondary FSBB integrated bridge is kept at about 0.9. While, the ac voltage gain gradually decreases from 0.93 to 0.45 with the charging power reducing from 150 to 30 W. The average current of the secondary bridge inductor  $L_{bs}$  is less than 0 as all power flows into the battery. Since the BIPT system operates on the positive half of the horizontal axis in Fig. 8, only MOSFET  $S_{s2}$  loses ZVS turn-ON.

3) *Simultaneous Charging of SC and Battery*: The experimental waveforms of simultaneous charging of SC and battery with 75 W when  $V_{sc} = 48$  V are shown in Fig. 18. The average current of the secondary inductor  $I_{Lbs\_avg}$  is about zero as no power flows between the SC and battery. Since the system with this charging mode operates in region I of Fig. 8, all MOSFETs in the system can realize ZVS turn-ON. Thus, the BIPT system has a higher efficiency in this mode compared to just charging the battery or SC.

4) *Backward Power Transfer*: Fig. 19 shows the experimental waveforms of the BIPT system prototype when the power is transferred from secondary side to primary source. Contrary to the forward power transmission, the phase angle  $\theta$  is set to  $-\pi/2$  for the backward power transfer, and the average current of the primary inductor  $I_{Lbp\_avg}$  is less than 0. In Fig. 20(a), the average current of the secondary inductor  $I_{Lbs\_avg}$  is greater than 0 due to the power discharged by the battery. Whereas in Fig. 19(c), the power is mainly supplied by the SC, so the inductor current is less than 0.

5) *Mode Switching*: The experimental mode switching waveforms of the secondary FSBB integrated bridge with HESS are presented in Fig. 20. Since the LCC-LCC compensation network is a constant-current topology and  $P_{ac}$  is kept at 150 or -150 W, the current  $i_{acs}$  does not vary during the switching process. The variation among different modes is reflected in the

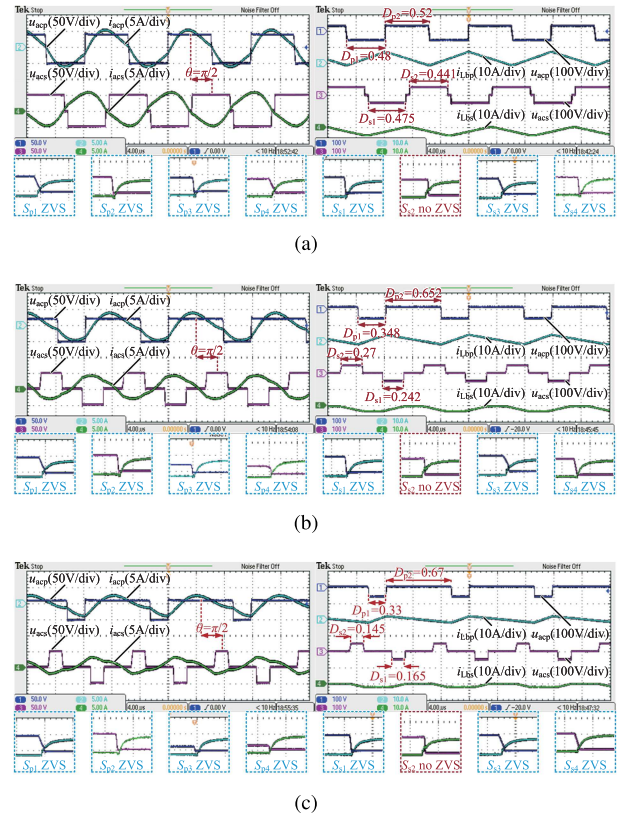


Fig. 17. Experimental waveforms of the battery charging when  $V_{sc} = 48$  V. (a) Full load ( $P_{bat} = 150$  W). (b) Half load ( $P_{bat} = 75$  W). (c) One-fifth load ( $P_{bat} = 30$  W).

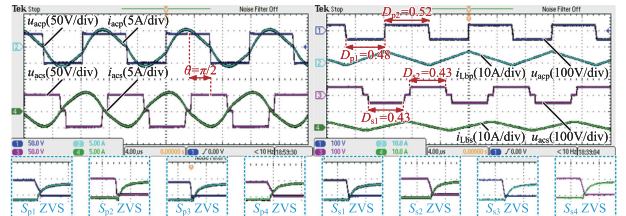


Fig. 18. Experimental waveforms of simultaneous charging of SC and battery when  $V_{sc} = 48$  V ( $P_{bat} = 75$  W,  $P_{sc} = 75$  W).

changing of inductor's average current from negative to positive or vice versa.

6) *Power Flow Between SC and Battery*: When the circuit of primary side is removed, the secondary FSBB integrated bridge has the flexibility to modulate power between SC and battery. Fig. 21 shows the experimental waveforms in this operation. Obviously, the secondary current  $i_{acs}$  fluctuates a bit but has an rms value of 0, so there is no active power in the secondary coil. The positive or negative value of the average inductor current  $i_{Lbs}$  represents the direction of power flow between the SC and the battery.

## B. Efficiency and Comparison

Fig. 22 plots curves of the system's measured efficiency versus SC voltage when SC is charged and discharged. In this

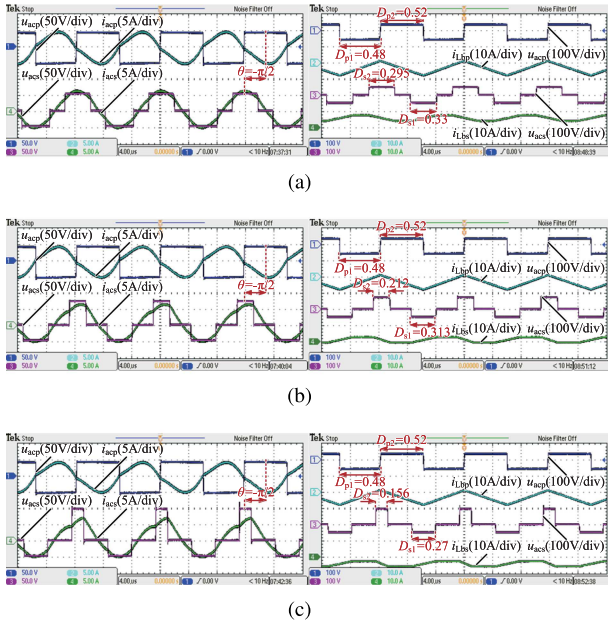


**Fig. 19.** Experimental waveforms of backward power transfer. (a)  $P_{sc} = 0$  W when  $V_{sc} = 48$  V. (b)  $P_{sc} = -75$  W,  $P_{bat} = -75$  W when  $V_{sc} = 72$  V. (c)  $P_{sc} = -150$  W when  $V_{sc} = 96$  V.

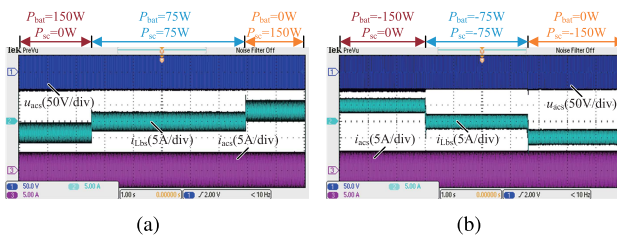


**Fig. 20.** Mode switching waveforms of secondary FSBB integrated bridge when  $V_{sc} = 48$  V. (a) Forward power transfer. (b) Backward power transfer.

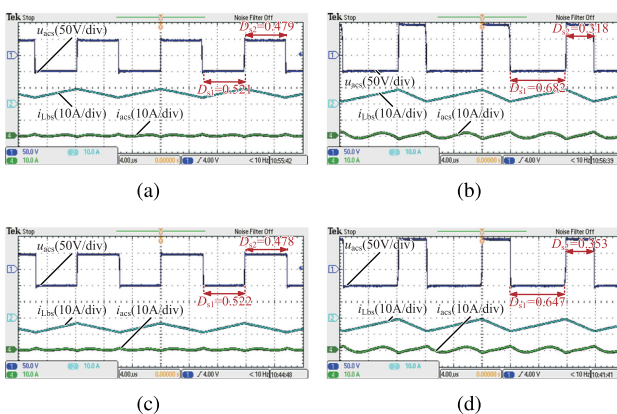


**Fig. 21.** Experimental waveforms of 150 W power flow between SC and battery when primary circuit is removed. (a) SC charging battery when  $V_{sc} = 48$  V. (b) SC charging battery when  $V_{sc} = 96$  V. (c) Battery charging SC when  $V_{sc} = 48$  V. (d) Battery charging SC when  $V_{sc} = 96$  V.

figure, ■ and ★ represent the system's efficiency of 150 W SC charging and discharging by the primary source, and ● and ◆ represent the system's efficiency of simultaneous 75 W SC and 75 W battery charging and discharging. Clearly, the maximum

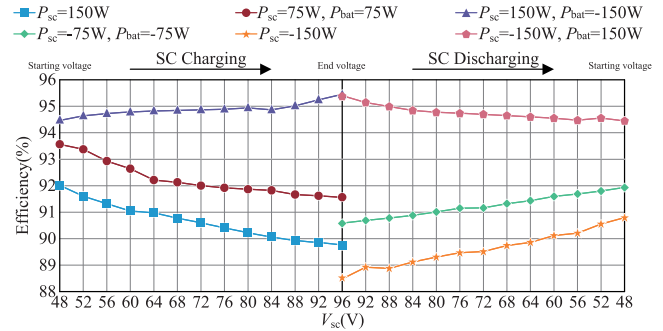


**Fig. 22.** Measured efficiency versus SC's voltage when SC is charged and discharged.

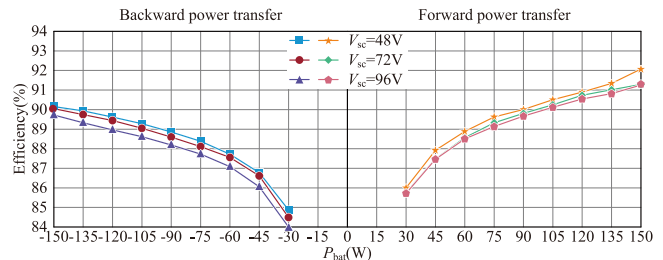


**Fig. 23.** Measured efficiency of the battery charging and discharging.

efficiency is 93.45%, and the efficiency of the system decreases with the increasing SC terminal voltage. This is because the reduction of the duty cycles with SC voltage leads to the increase in the rms currents and turn-OFF currents of the MOSFETs. ▲ and ★ in this figure represent the efficiency of the secondary FSBB integrated bridge with power interaction between SC and battery when the primary circuit is removed. Obviously, the efficiency of the secondary FSBB integrated bridge can be maintained at about 95% in this operation mode.

Fig. 23 illustrates the system's efficiency when the SC terminal voltage is constant and only the battery is charged or discharged. It can be seen that the maximum efficiency of 92% occurs when the battery is charged at 150 W. As the charging power decreases, there is an inevitable drop in the system's efficiency. While the overall efficiency can be maintained above 84%. In both figures, the efficiency of forward power transfer is higher than that of backward power transfer. This is because the MOSFETs' turn-OFF currents increase with the decreasing of duty cycles  $D_{s1}$  and  $D_{s2}$ , leading to the rise of MOSFETs' turn-OFF losses. It thus accounts for a larger percentage of the total losses during the backward power transfer. Using GaN transistors with better dynamic characteristics can effectively reduce turn-OFF losses, but this comes with additional costs.

To compare the work presented in this article with other topologies for wireless charging of HESS, Table II summarizes the articles cited in this article from the perspective of separate power control of battery and SC ability, maximum efficiency, and number of power conversion stages, semiconductor devices, and inductors at the secondary side. It is evident that the proposed BIPT system with FSBB integrated bridges can realize separate power control of SC and battery utilizing only one inductor and four MOSFETs. In addition, the maximum

**TABLE II**  
COMPARISON OF TOPOLOGIES FOR WIRELESS CHARGING OF HESS

Paper reference	This work	[14]	[15]	[16]	[17]	[18]
Separate power control of SC and battery	YES	NO	YES	YES	YES	YES
Number of conversion stages	1	2	4	3	2	1
Number of mosfets	4	6	6	4	4	4
Number of diodes	0	0	4	4	0	0
Number of inductors	1	2	3	2	1	2
Maximum efficiency (%)	93.45	N/A	90	93	72.3	N/A

transmission efficiency of 93.45% of the BIPT system is greater than that of most IPT systems.

## VI. CONCLUSION

In this article, an FSBB integrated bridge is proposed for combining the BIPT system with HESS. By multiplexing the half-bridges in the FSBB topology, the proposed FSBB integrated bridge has two dc ports with adjustable dc voltage gain for HESS and an ac port with adjustable ac voltage gain for BIPT system. Thus, energy can flow freely and effectively among the battery, SC, and the primary source. Together with the proposed modulation method and control strategy, the BIPT system with FSBB integrated bridges for HESS can achieve the maximum efficiency of 93.45%. When the primary circuit is removed, the maximum efficiency of the power flow between the SC and the battery is 95.4%.

## REFERENCES

- G. Buja, M. Bertoluzzo, and K. N. Mude, "Design and experimentation of WPT charger for electric city car," *IEEE Trans. Ind. Electron.*, vol. 62, no. 12, pp. 7436–7447, Dec. 2015.
- D. Patil, M. K. McDonough, J. M. Miller, B. Fahimi, and P. T. Balsara, "Wireless power transfer for vehicular applications: Overview and challenges," *IEEE Trans. Transp. Electrific.*, vol. 4, no. 1, pp. 3–37, Mar. 2018.
- M. Yilmaz and P. T. Krein, "Review of battery charger topologies, charging power levels, and infrastructure for plug-in electric and hybrid vehicles," *IEEE Trans. Power Electron.*, vol. 28, no. 5, pp. 2151–2169, May 2013.
- W. Liu, K. T. Chau, C. C. T. Chow, and C. H. T. Lee, "Wireless energy trading in traffic Internet," *IEEE Trans. Power Electron.*, vol. 37, no. 4, pp. 4831–4841, Oct. 2022.
- Y. Liu, C. Liu, W. Wang, S. Liu, and Y. Chen, "A novel wired/wireless hybrid multiport energy router for dynamic EV energy Internet with grid-tied and islanded operations," *IEEE Trans. Ind. Electron.*, vol. 71, no. 4, pp. 3559–3571, May 2024.
- H. Zhang, F. Lu, and C. Mi, "An electric roadway system leveraging dynamic capacitive wireless charging: Furthering the continuous charging of electric vehicles," *IEEE Electricif. Mag.*, vol. 8, no. 2, pp. 52–60, Jun. 2020.
- K. Clement-Nyns, E. Haesen, and J. Driesen, "The impact of charging plug-in hybrid electric vehicles on a residential distribution grid," *IEEE Trans. Power Syst.*, vol. 25, no. 1, pp. 371–380, Feb. 2010.
- J. B. Goodenough and Y. Kim, "Challenges for rechargeable Li batteries," *Chem. Mater.*, vol. 22, no. 3, pp. 587–603, Aug. 2010.
- A. Burke, "Ultracapacitors: Why, how, and where is the technology," *J. Power Sources*, vol. 91, no. 1, pp. 37–50, Nov. 2000.
- A. F. Burke, "Batteries and ultracapacitors for electric, hybrid, and fuel cell vehicles," *Proc. IEEE*, vol. 95, no. 4, pp. 806–820, Apr. 2007.
- A. Khaligh and Z. Li, "Battery, ultracapacitor, fuel cell, and hybrid energy storage systems for electric, hybrid electric, fuel cell, and plug-in hybrid electric vehicles: State of the art," *IEEE Trans. Veh. Technol.*, vol. 59, no. 6, pp. 2806–2814, Apr. 2010.
- M. Ortuzar, J. Moreno, and J. Dixon, "Ultracapacitor-based auxiliary energy system for an electric vehicle: Implementation and evaluation," *IEEE Trans. Ind. Electron.*, vol. 54, no. 4, pp. 2147–2156, Jul. 2007.
- J. Shen, S. Dusmez, and A. Khaligh, "Optimization of sizing and battery cycle life in battery/ultracapacitor hybrid energy storage systems for electric vehicle applications," *IEEE Trans. Ind. Informat.*, vol. 10, no. 4, pp. 2112–2121, Jul. 2014.
- S. S. Pasupuleti, N. R. Tummuru, and H. Misra, "Power management of hybrid energy storage system based wireless charging system with regenerative braking capability," *IEEE Trans. Ind. Appl.*, vol. 59, no. 3, pp. 3785–3794, Jan. 2023.
- M. McDonough, "Integration of inductively coupled power transfer and hybrid energy storage system: A multiport power electronics interface for battery-powered electric vehicles," *IEEE Trans. Power Electron.*, vol. 30, no. 11, pp. 6423–6433, Apr. 2015.
- Y. Geng, Z. Yang, and F. Lin, "Design and control for catenary charged light rail vehicle based on wireless power transfer and hybrid energy storage system," *IEEE Trans. Power Electron.*, vol. 35, no. 8, pp. 7894–7903, Jan. 2020.
- S. Ruddell, U. K. Madawala, and D. J. Thrimawithana, "Dynamic WPT system for EV charging with integrated energy storage," *IET Power Electron.*, vol. 12, no. 10, pp. 2660–2668, Aug. 2019.
- S. Ruddell, U. K. Madawala, and D. J. Thrimawithana, "A wireless EV charging topology with integrated energy storage," *IEEE Trans. Power Electron.*, vol. 35, no. 9, pp. 8965–8972, Jan. 2020.
- X. Ren, X. Ruan, H. Qian, M. Li, and Q. Chen, "Three-mode dual-frequency two-edge modulation scheme for four-switch buck-boost converter," *IEEE Trans. Power Electron.*, vol. 24, no. 2, pp. 499–509, Feb. 2009.
- R. Mai, Y. Liu, Y. Li, P. Yue, G. Cao, and Z. He, "An active-rectifier-based maximum efficiency tracking method using an additional measurement coil for wireless power transfer," *IEEE Trans. Power Electron.*, vol. 33, no. 1, pp. 716–728, Feb. 2018.
- S. Li, W. Li, J. Deng, T. D. Nguyen, and C. C. Mi, "A double-sided LCC compensation network and its tuning method for wireless power transfer," *IEEE Trans. Veh. Technol.*, vol. 64, no. 6, pp. 2261–2273, Aug. 2015.
- X. Zhang et al., "A control strategy for efficiency optimization and wide ZVS operation range in bidirectional inductive power transfer system," *IEEE Trans. Ind. Electron.*, vol. 66, no. 8, pp. 5958–5969, Aug. 2019.
- I.-W. Iam, C.-K. Choi, C.-S. Lam, P.-I. Mak, and R. P. Martins, "A constant-power and optimal-transfer-efficiency wireless inductive power transfer converter for battery charger," *IEEE Trans. Ind. Electron.*, vol. 71, no. 1, pp. 450–461, Jan. 2024.
- F. Liu, J. Xu, Z. Chen, R. Huang, and X. Chen, "A constant frequency ZVS modulation scheme for four-switch buck-boost converter with wide input and output voltage ranges and reduced inductor current," *IEEE Trans. Ind. Electron.*, vol. 70, no. 5, pp. 4931–4941, Jul. 2023.



**Chunwei Ma** (Graduate Student Member, IEEE) received the B.Eng. degree in electrical engineering from Nanjing Institute of Technology, Nanjing, China, in 2017, and the M.Eng. degree in power electronics from Nanjing University of Science and Technology, Nanjing, in 2020. He is currently working toward the Ph.D. degree in electrical engineering with the Southeast University, Nanjing.

From 2020 to 2021, he was a Hardware Engineer with Da-Jiang Innovations (DJI), Shenzhen, China. His research interests include wireless power transfer, power factor correction converters, and motor drives.



**Xiaohui Qu** (Senior Member, IEEE) received the B.Eng. and M.Eng. degrees in electrical engineering from Nanjing University of Aeronautics and Astronautics, Nanjing, China, in 2003 and 2006, respectively, and the Ph.D. degree in power electronics from The Hong Kong Polytechnic University, Hong Kong, China, in 2010. Since 2010, she has been with the School of Electrical Engineering, Southeast University, Nanjing, where she is currently a Full Professor with a research focus on power electronics. In 2009, she was engaged as a Visiting Scholar with the Center for Power Electronics Systems, Virginia Tech, VA, USA. From 2015 to 2016, she was a Visiting Scholar with the Center of Reliable Power Electronics (CORPE), Aalborg University, Aalborg, Denmark. Her research interests include wireless power transfer, flexible ac/dc distribution power system, and power electronics reliability.

Dr. Qu was the recipient of the Outstanding Reviewer Award in 2017 and the Prize Paper Awards in 2017 and 2022, respectively, by IEEE TRANSACTIONS ON POWER ELECTRONICS. She is an Associate Editor of IEEE TRANSACTIONS ON POWER ELECTRONICS and *CPSS Transactions on Power Electronics and Applications*.



**Zhihao Guo** received the B.Eng. degree in electrical engineering and automation from Shandong University of Science and Technology, Qingdao, China, in 2019, and the M.Eng. degree in electrical engineering from Qingdao University, Qingdao, in 2023. He is currently working toward the Ph.D. degree in electrical engineering with the Southeast University, Nanjing, China.

His research interest includes wireless power transfer.



**Linlin Tan** (Member, IEEE) received the B.S. degree in electrical engineering and automation from Harbin Engineering University, Harbin, China, in 2008, and the Ph.D. degree in electrical engineering from the Southeast University, Nanjing, China, in 2014.

Currently, he is an Associate Professor with the School of Electrical Engineering, Southeast University. He has authored or co-authored more than 50 papers and more than 50 inventions. His research interests include wireless power transfer, wireless charging for electric vehicles, and wireless V2G.